Geological and geochemical data from the proposed Sirente crater field: New age dating and evidence for heating of target

Jens ORMÖ[1]*, Christian KOEBERL[2], Angelo Pio ROSSI[3, 4], and Goro KOMATSU[3]

[1]Centro de Astrobiología (CSIC/INTA), Instituto Nacional de Técnica Aeroespacial, Ctra de Torrejón a Ajalvir, km 4, 28850 Torrejón de Ardoz, Madrid, Spain
[2]Department of Geological Sciences, University of Vienna, Althanstrasse 14, A-1090 Vienna, Austria
[3]International Research School of Planetary Sciences, Universita d'Annunzio, Viale Pindaro 42, 65127 Pescara, Italy
[4]ESA Research and Scientific Support Department, Keplerlaan 1, Postbus 299, ESTEC/SCI-SB, 2200 AG Noordwijk, The Netherlands
*Corresponding author. E-mail: ormo@inta.es

Abstract–The proposed Sirente crater field consists of a slightly oblong main structure (main crater) 120 m in width and about 30 smaller structures (satellite craters), all in unconsolidated but stiff carbonate mud. Here we focus on the subsurface structure of the satellite craters and compare the Sirente field with known meteorite crater fields. We present a more complete outline of the crater field than previously reported, information on the subsurface morphology of a satellite crater (C8) 8 m in width, radiocarbon and thermoluminescence (TL) ages of material from this crater, and evidence for heated material in both crater C8 and the rim of the main crater. Crater C8 has a funnel shape terminating downwards, and evidence for soil injection from the surface to a depth of 9 m. The infill contained dispersed charcoal and small, irregular, porous fragments of heated clay with a calibrated age of B.P. 1712 (^{13}C-corrected radiocarbon age: B.P. 1800 ± 100) and a TL age of B.P. 1825 (calculated error ±274). Together with previous radiocarbon age (B.P. 1538) of the formation of the main crater (i.e., target surface below rim), a formation is suggested at the beginning of the first millennium A.D. Although projectile vaporization is not expected in Sirente-sized craters in this type of target material, we used geochemistry in an attempt to detect a meteoritic component. The results gave no unequivocal evidence of meteoritic material. Nevertheless, the outline of the crater field, evidence of heated material within the craters, and subsurface structure are comparable with known meteorite crater fields.

INTRODUCTION

Background and Aim of Study

Recently, a group of depressions and a subcircular, rimmed lake in a high valley in the Central Apennines was proposed to have formed by meteoritic impact (Ormö et al. 2002). Since then, the rimmed lake has been suggested to be simply an anthropogenic cattle pond in a field of karstic sags (Speranza et al. 2004), or a consequence of a new mechanism for mud volcano formation involving mud-fountaining (Stoppa 2006). Our study aims to provide more geological data for the evaluation of the different hypotheses. For simplicity in making comparisons with known impact structures, we have chosen to use the term "crater" for all the depressions in the proposed crater field, although the mode of origin has not yet been confirmed.

The rimmed lake (main crater) is located in one end of the field of minor depressions (satellite craters) (Fig. 1). It has a slightly elongated outline with a mean diameter of 120 m (Ormö et al. 2002). Its rim is saddle-shaped (i.e., higher on the longer sides of the ellipse) and rises at a maximum of 2.2 m above the surrounding plain. However, the original surface on top of which the rim has been emplaced (i.e., the target surface) is at this location about 1 m below the present surface of the plain (Ormö et al. 2002). Drilling and trenching of the rim by Ormö et al. (2002) and for this study have shown an overturning of material consistent with an impact formation. The studies have not shown any features that would indicate shoveling by humans (e.g., chaotically distributed chunks of paleosol), or any structures indicating that the rim was built up by cyclic flows (cf. Stoppa 2006).

The small craters have an apparent depth of 1.5–2 m. Some have slightly elevated rims, but most are only shallow, rimless, flat-floored, circular depressions (Fig. 2).

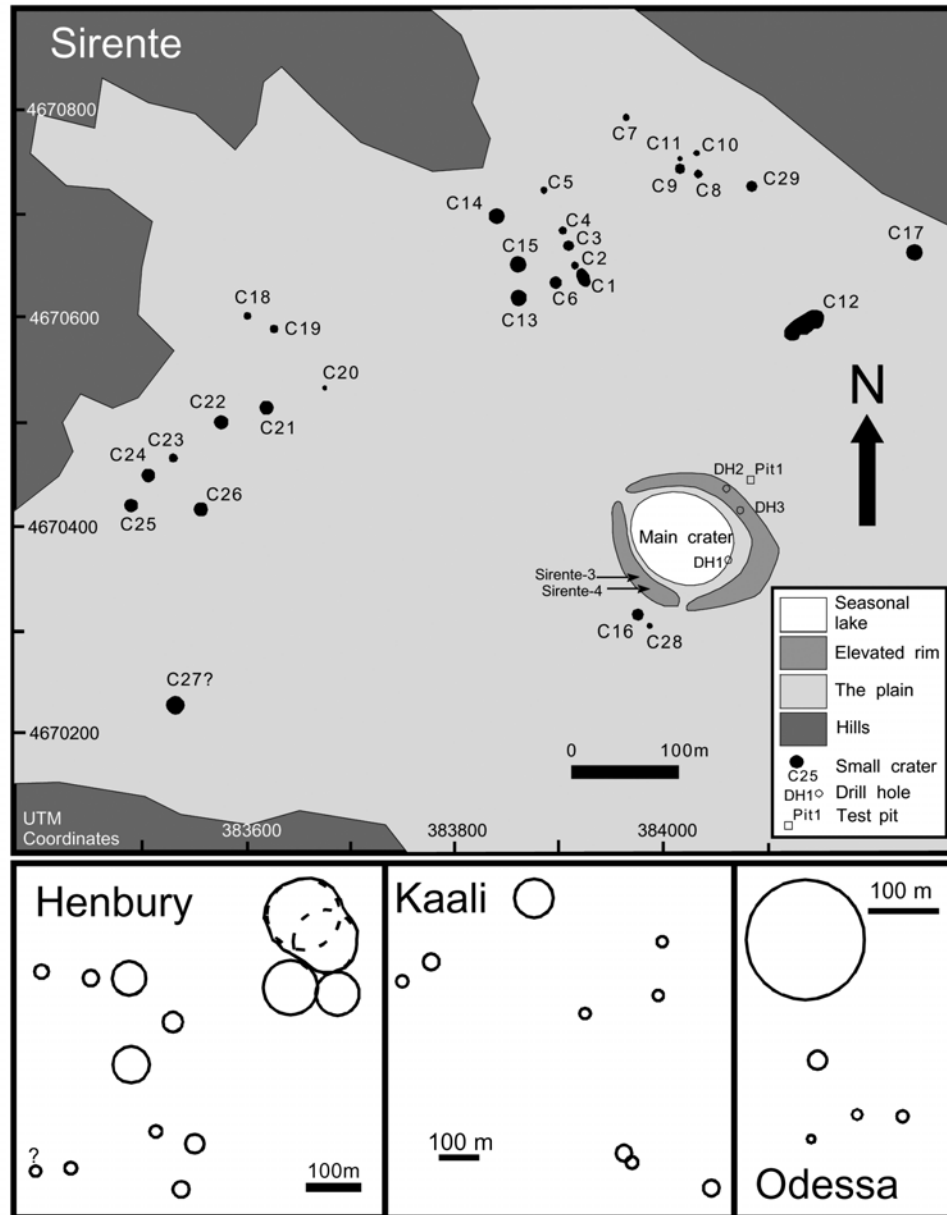Accelerator mass spectrometry (AMS) dating of organic

Fig. 1. An outline of the Sirente crater field. Sampling sites are indicated. The outlines of the Henbury (Milton 1968), Kaali (Hodge 1994 and references therein), and Odessa (Evans 1961) crater fields are given for reference.

soil from the proposed target surface below the material of the rim of the largest crater (main crater) suggests that it formed around B.P. 1538 (4th–5th century A.D.) (Ormö et al. 2002) (Table 1), which is coeval with a local legend from the nearby town of Secinaro (Santilli et al. 2003). The legend was recorded by the local church and describes people at the Sirente Mountain witnessing an approaching star that soon outshines the sun. Its apparent impact generates an earthquake, rupturing the local temple and knocking people to the ground. The people recover an object, which then is placed on the altar of their new church.

Standard characteristics required to confirm an impact origin are evidence of shock metamorphism and/or the presence of traces of meteoritic material in breccias or melt rocks (or meteorite fragments) (cf. French 1998; Montanari and Koeberl 2000). However, the confirmation of shock metamorphism at Sirente is difficult because a) shock pressures may be too low to produce unique shock metamorphic effects (cf. Koeberl et al. 1998), b) the target at Sirente is a carbonate mud almost completely devoid of minerals useful for studies of shock metamorphic features, and c) mineral grains embedded in soft porous matrix (e.g., clay and carbonate mud) experience lower shock pressures than those in solid rock (Kenkmann and Dresen 1998). Ormö
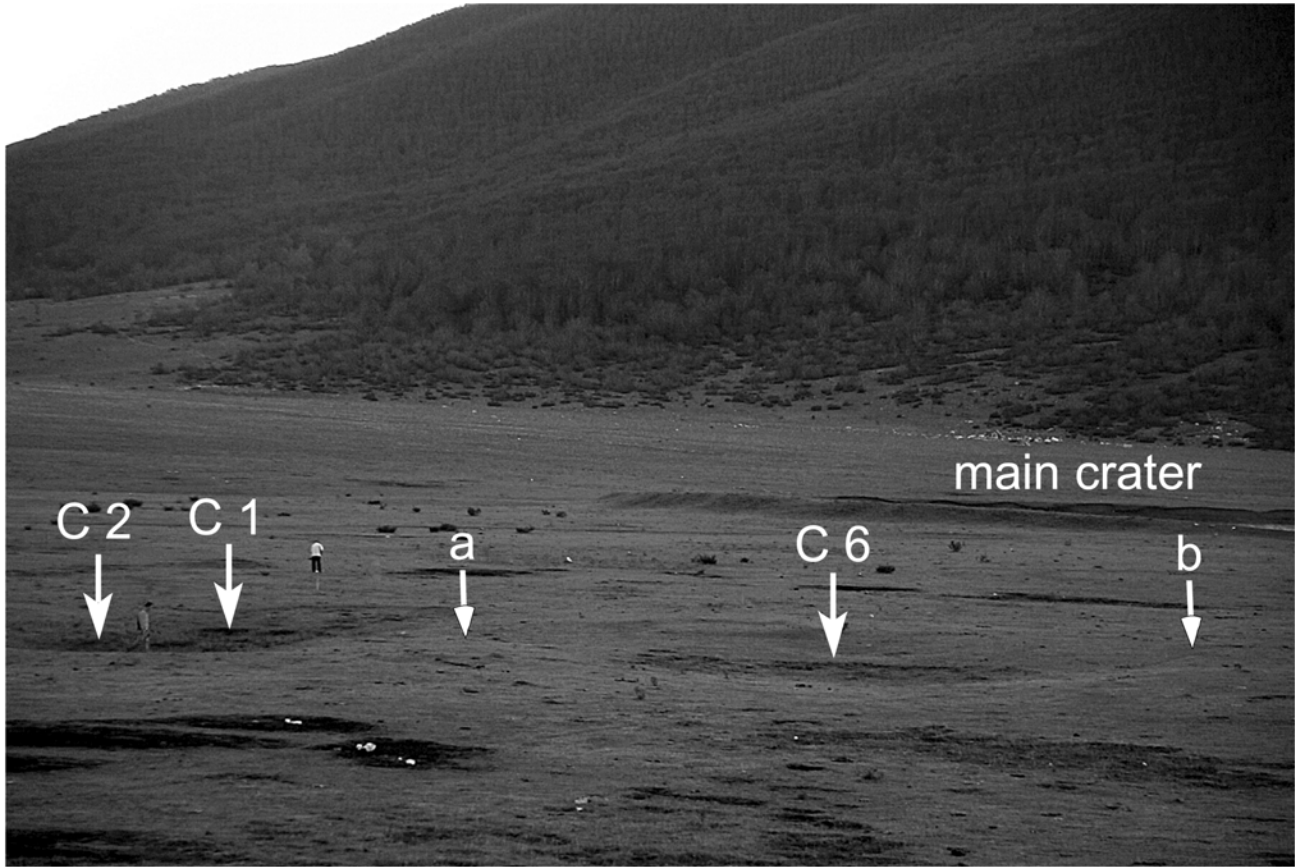
Fig. 2. The surface appearance of individual craters. Arrows (a) and (b) around crater C6 indicate the rim. The main crater is visible in the background. Note persons at craters C1 and C2 for scale.

et al. (2002) report fractured feldspar and pyroxene grains in material from the main crater rim. However, the level of deformation is not diagnostic for impact. Thus, only the recovery of meteoritic material can prove an impact origin for the Sirente crater field (see discussion below).

The main objective of this study is the outline of the crater field, its age, and the subsurface structure of the satellite craters. The results are compared with known meteorite crater fields. We have also searched for macroscopic and geochemical traces of meteoritic material.

Geological Setting and Historical Context

No bedrock crops out within the Sirente plain. The valley is a fault-controlled (extensional) basin. All the craters, including the main crater, are developed entirely in yellowish, unconsolidated but stiff carbonate mud of likely lacustrine origin with sporadic organic-rich and clay-rich horizons (cf. Giraudi 1997). The few mineral grains that can be retrieved after dissolution of the sediment in acid may be tephra (Ormö et al. 2002). The bedrock exposed on nearby hills consists of tectonized shallow-marine sediments, mainly limestones. The area is tens of kilometers from any past or present volcanic

centers. Coarser material and even large limestone boulders from the nearby mountain scarp occur sporadically in the sediments of the plain and in the rim of the main crater. Ormö et al. (2002) reported two large (a few cubic meters), strongly fractured limestone boulders on the apparent crater floor near the southwestern rim. The occurrence of the boulders within the crater is considered by both Speranza et al. (2004) and Stoppa (2006) as crucial evidence against the impact hypothesis. However, in the impact scenario, these boulders existed within the target sediments and were simply emplaced on, or within, the rim by the low-velocity tail of the excavation flow and, subsequently, slid back to their present position (cf. Melosh 1989, Fig. 6.1).

More extensive coarse-clastic alluvial deposits cover the eastern half of the plain (Servizio Geologico d'Italia-APAT, Forthcoming). These alluvial sediments were called "calcareous breccias" by Speranza et al. (2004) despite the fact that they form loose deposits and not a rock, which is important to the discussion regarding karst features. There are no crater-like depressions in the eastern part of the plain.

Speranza et al. (2004) argued for an anthropogenic origin for the Sirente structure by stating that it is situated along an ancient route for herding sheep ("tratturi"), citing a popular

Table 1. Ages of material from the Sirente crater field. The term "target surface" refers to the top of the soil onto which the rim material has been deposited. Samples marked with * were previously published by Ormö et al. (2002). Only samples C8_T1_2.2, C8_charcoal_1.8, and DH2(1.5) may, theoretically, have ages directly linked to the formation of the respective crater. The ages of the other samples are used for constraining the time of formation.

Sample number	Sample description and interpretation	Method	Radiocarbon age (B.P.) ^{13}C-corrected	Calibrated ages from intercepts (B.P.) and TL age (B.P.)
C8_T1_2.2	Heated clay in crater C8. Age of impact or older.	TL		1825 ± 274
C8_charcoal_1.8	Charcoal in crater C8. Age of impact or older.	[14]C (extended counting time)	1800 ± 100	1σ: 1865–1571 2σ: 1948–1519
DH2(0.9)*	Organic soil within the rim material above the "target surface." Overturned flap of material older than the impact.	[14]C	2560 ± 120	1σ: 2775–2364 2σ: 2918–2344
DH2(1.5)*	Top of organic soil ("target surface"). Age of impact.	AMS	1650 ± 40	1σ: 1591–1521 2σ: 1689–1418
DH2(2.0)*	Organic soil horizon below the "target surface." Older than impact.	[14]C (extended counting time)	2490 ± 170	1σ: 2761–2344 2σ: 2946–2124
C9(3.5)org*	Soil fragment in crater C9. Much older than impact, but relocated by the impact.	[14]C	3810 ± 90	1σ: 4405–4019 2σ: 4494–3926

book on the matter. This information is contradicted by information given in maps of the Central Board of Regional Antiquities and Archaeology (Soprintendenza). There are no routes related to ancient sheep movements within 10 km of Prati del Sirente (Commissariato per la reintegra dei tratturi di Foggia 1959; Soprintendenza per i Beni Archeologici per L'Abruzzo 2004). Moreover, these shepherd routes are usually located at lower altitudes than Prati del Sirente.

EXPERIMENTAL METHODS

Mapping of the Crater Field

The mapping follows the method of Ormö et al. (2002). The diameters of the dots that show the location of each crater in Fig. 1 only indicate the diameter of the obvious depression within each structure. The rim diameter may be larger, as illustrated in Fig. 2 for crater C6.

Machine Excavation and Sampling

One of the satellite craters (C8) in the crater field was excavated with a machine excavator. All removed material was examined visually and with a metal detector. The excavation was initially performed level by level, making a vertical profile approximately 20 m long and 3 m deep through the crater (Fig. 3). After that, to be able to reach a greater depth, the whole upper part of the crater had to be removed to create a platform 3 m deep and 20 × 30 m wide. The excavation then continued within a shaft 3 × 3 m wide to a depth of 9 m, where the excavation had to stop due to economic and safety reasons.

The main crater rim was investigated with small-scale trenching. Pedogenesis has reached a depth of about 1–1.5 m
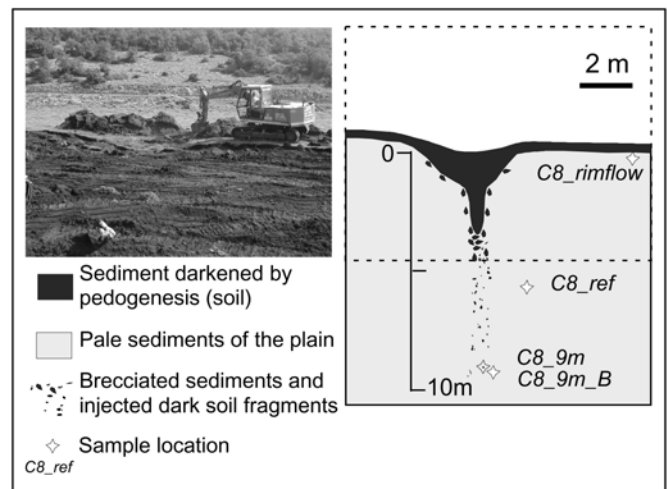

Fig. 3. A schematic profile of crater C8. The photo to the left shows the location of C8 at the beginning of excavation. A profile is created passing straight through the crater.

on the rim of the main crater since its formation, which is slightly deeper than the 0.7–1 m for the rest of the plain (Ormö et al. 2002). A pit was dug 0.5 m deep into the inner side of the elevated rim approximately 1 m below the rim crest (Sirente-3). A second sample (Sirente-4) was taken in a similar position on the inward-facing wall of the crater rim approximately 10 m along the rim eastward from Sirente-3. Following the procedure of treatment with HCl described by Ormö et al. (2002), five kg of the carbonate mud and clay material from Sirente-3 gave a residue with the dry weight of 2.4 g. To ascertain that the acid treatment does not affect the appearance of the residue, we made a test by first treating only half of the sample with HCl. Reference material from the plain unaffected by a putative impact event (sample C8_Ref)
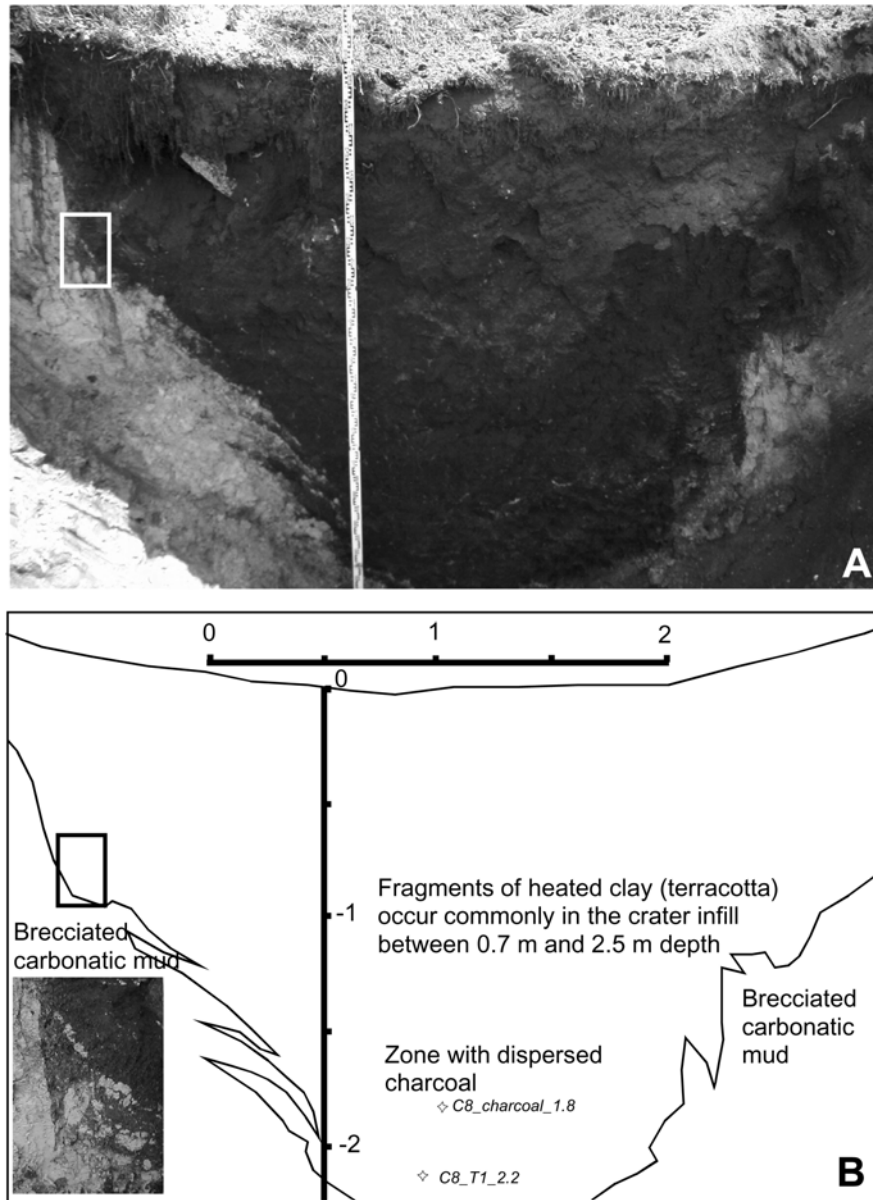
Fig. 4. A profile of crater C8. Pedogenesis has transferred the infill of the depression into a dark soil. Irregular fragments and patches of grains of rust-colored heated clay and fragments of charcoal are common in the dark soil of the bowl-shaped part (Fig. 5). Inset frame shows rupture of the pale carbonate mud hosting the structure.

was also investigated with the same method. All samples were taken with a plastic scoop (for sample locations, see Figs. 1, 3, and 4). For the location of samples taken in the previous study and discussed in the present paper, see Ormö et al. (2002).

Age Dating

Radiocarbon

Samples from C8 were radiocarbon-dated at Geochron Laboratories, USA (which selected the preferred method for each sample). Sample C8_charcoal_1.8 contained charcoal that was dated. The charcoal fragments were separated from sand, silt, rootlets, and foreign matter. The sample was then treated with hot dilute 1N HCl to remove any carbonates, with 0.1N dilute NaOH to remove humic acids and other organic contaminants, and a second time with dilute HCl. The sample was then rinsed and dried and the cleaned charcoal was combusted to CO_2 and then from CO_2 was synthesized CH_4. This yielded only 0.5 g of carbon as CH_4, which had to be measured for 100 h to decrease the error down to 100 yr. Sample C9(3.5)org (radiocarbon age by Ormö et al. (2002) discussed here) was dispersed in a large volume of water, which was passed through a fine nylon mesh to filter out any
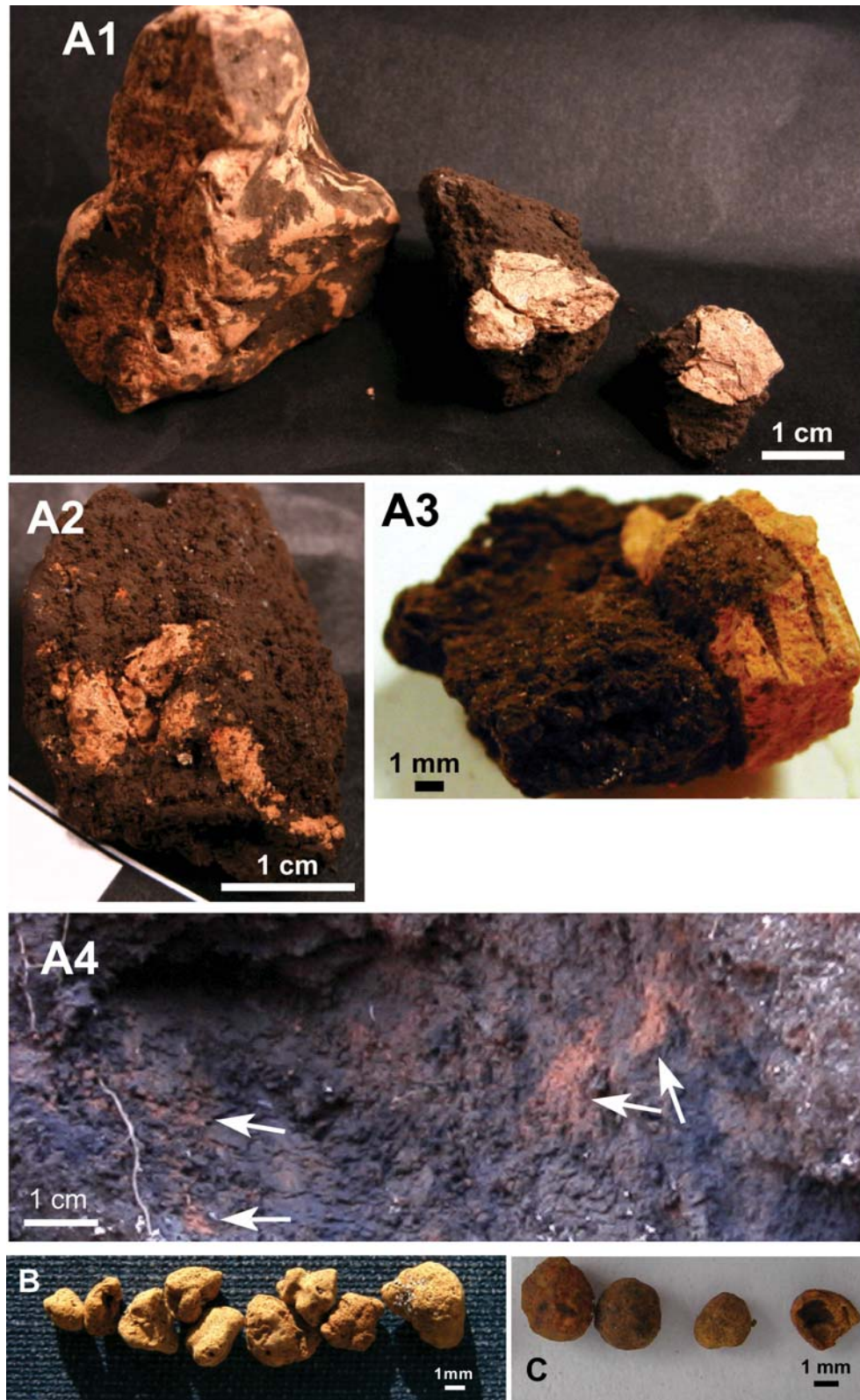
Fig. 5. Heated clay from crater C8 (figures labeled a), heated clay fragments (b), and spherical "rusty crusts" (c) from the elevated rim of the main crater. The largest fragment in (a1) was dated with TL method. Note porous appearance and root holes in the lower part. Most fragments are as weak as the surrounding sediment and form an irregular and gradual transition (a2) to the host sediment. Extension fractures in (a3) may indicate rapid heating. In many places, the heated clay is only visible as a rust-coloring of the dark host sediment (a4).

particulates. The organic fraction was then treated with hot dilute 1N HCl for one hour to dissolve any carbonates. After filtering, washing, and drying, the organic fraction was then combusted in pure oxygen to produce CO_2 and subsequent CH_4 for the analysis. Samples DH2(0.9) and DH2(2.0), as well as DH2(1.5) (ages published by Ormö et al. (2002) and discussed here) were treated in the same way as C9(3.5)org, except that DH2(1.5) was decanted instead of filtered, and analyzed by AMS. The results were calibrated by Geochron Laboratories with a program by Stuiver and Reimer (1993), using the calibration file from Stuiver et al. (1998). The radiocarbon ages are based on the Libby half-life (5570 years) for ^{14}C. The error is ±1 s as judged by the analytical data alone. The modern standard is 95% of the activity of N.B.S. Oxalic Acid. The age (B.P.) is referenced to the year A.D. 1950. Calibrated age ranges are obtained by intercept method.

Thermoluminescence (TL)

Methods and data reduction for our thermoluminescence analyses follow those of Aitken (1985). After the sample (C8_T1_2.2, shown to the left in Fig. 5A1) had been retrieved from its 2.2 m deep location in crater C8, it was placed in a plastic bag and a box to avoid unnecessary exposure to sunlight. The sample was analyzed at the Rathgen-Forschungslabor, Berlin, Germany. About 3.5 g of interior sample material was ground to a grain size of 1–10 µm. After HCl cleaning, the 2–10 µm-size fraction was isolated by sedimentation in acetone. The fraction contained predominantly quartz, feldspar, and some iron minerals. Non-quartz minerals remaining after acid treatment do not contribute to the luminescence signal. The TL analysis was made with a Riso-DA-12 instrument and a ^{90}Sr source (Sick5100–Amersham). For the measurements of the environmental gamma dose-rate, an estimate was calculated from the alpha count-rate and the potassium content of the sample. Due to the depth from which the sample was taken (>2 m) the cosmic ray dose was neglected. A 20 rel% was calculated based on Aitken (1976). Conversion factors were given by Nambi and Aitken (1986). The temperature to which the sample had been heated before being deposited within the sediment was analyzed with re-firing technique (cf. Daszkiewicz and Schneider 2001) with the use of oxidizing atmosphere in electric oven.

Geochemical Analysis

Samples suspected to contain meteoritic component and reference samples were analyzed by X-ray fluorescence (XRF) spectrometry and instrumental neutron activation analysis (INAA) (see Reimold et al. 1994 and Koeberl 1993 for details on procedures, precision, and accuracy). Samples with suspected meteorite component were those that showed an anomalous rust-coloring as compared with the normal appearance of the sediments (see discussion below on rust-colored material observed at other impact sites), and material that could include ejected meteorite fragments (i.e., the main crater rim). The rust-colored material seems restricted to the funnel infill of the small investigated craters and the rim of the main crater where meteoritic material is most likely to occur. The following samples were analyzed: C8_Ref, which is a reference sample of pale, carbonate mud (lacustrine sediment) in which the craters have formed (i.e., target material); C9_3m, which is a sample of rust-colored dark soil from crater C9; C8_9m_B, which is a sample of rust-colored pale carbonate mud from crater C8; C8_TC2, which is a subsample (a piece) of sample C8_T1_2.2 (Fig. 5a4); Sirente-3_Bulk, which is bulk material (carbonate mud) from the elevated rim of main crater; Sirente-3_Residue, which consists of the remains after diluting and dissolving material from Sirente-3; and Sirente-4, which is rim material of the main crater more strongly affected by pedogenesis (dark with higher organic content).

RESULTS

Mapping of the Crater Field and Surface Morphology of Individual Craters

Ormö et al. (2002) estimated the crater field to be 450 m in length and 400 m wide, with 17 smaller craters distributed close to a main crater. In this study, we revise the first outline by the discovery of 11 additional structures (Fig. 1). The craters form three main groups in addition to a few sporadic occurrences. The area between the three clusters of craters and the main crater is hummocky, but without distinct crater-like depressions.

Subsurface Structure and Indications for Material Displacement at Crater C8

Crater C8 shows the same bowl-shaped upper part and "tunnel-like" continuation (i.e., "funnel crater," following terminology by Svettsov 1998) as noticed at crater C9 in the partial excavation by Ormö et al. (2002). Post-formational pedogenesis has colored the infill nearly black, which stands out in strong contrast to the pale, clay-like carbonate mud of the host material (Figs. 3 and 4). The apparent crater floor (i.e., the present ground surface at the center of the crater) is the reference level for all further depth values in this study, if not indicated otherwise. A steeply inclined "tunnel" less than a meter wide can be traced by its content of coherently dark-colored soil to about 4 m depth. Below that level, the tunnel is indicated by angular chunks of black paleosol that appear to have been dragged downwards. A zone with sharp, straight-edged rupture of the host sediment occurs at the interface between the dark infill and the pale host sediment down to the entrance of the tunnel (Fig. 4).

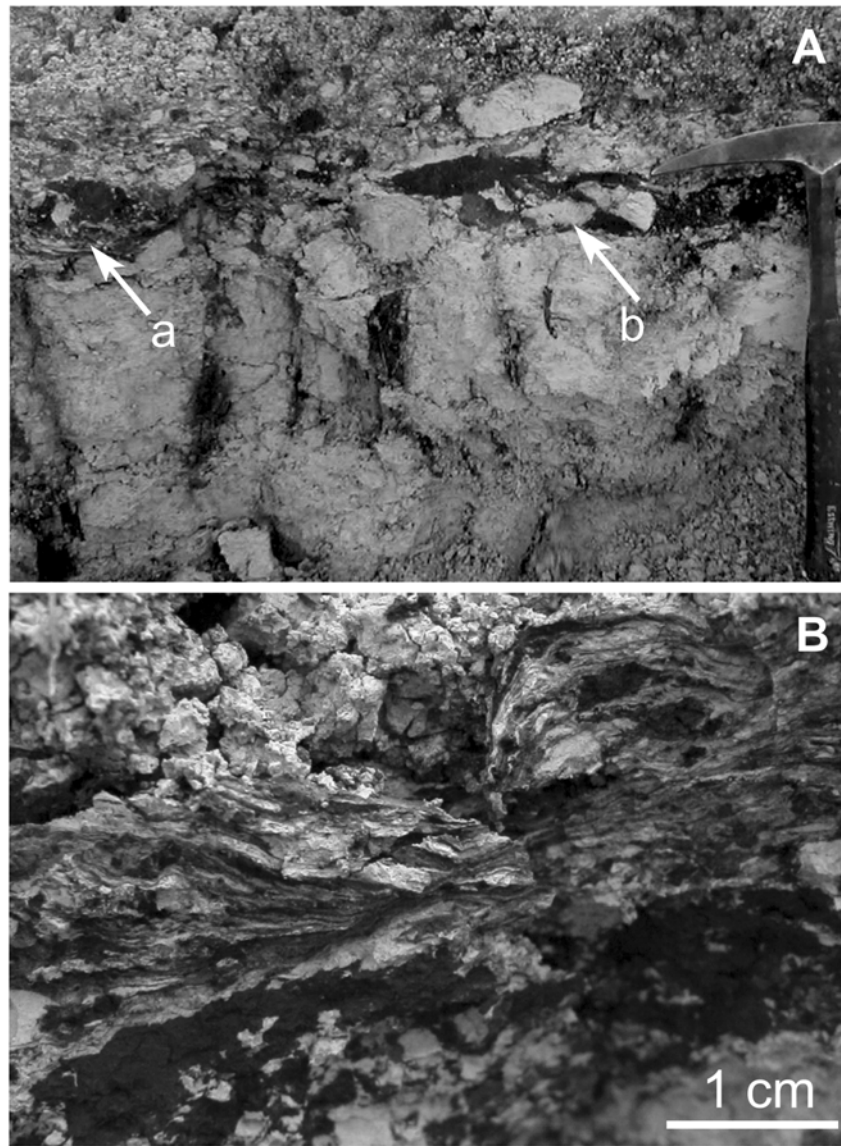At a position 70 cm below the plain's surface and 7 m

Fig. 6. a) Soil and sediment fragments in a matrix with sheared structures (C8_rimflow) outside the rim of C8 (see Fig. 3 for location). The arrows indicate a sharp contact toward less disturbed sediments. b) A close-up of section located at the left arrow (a) in Fig. 6a.

outside (east) of the crater center, a layer of soil breccia (black soil fragments and pale sediment fragments) with sheared matrix occurs discordant on top of the pale host sediments of the plain (sample C8_rimflow in Figs. 3 and 6). Below the breccia bed there are vertical, black-colored features that continue to a depth of 1.5 m. They decrease in number away from the crater. A sharp, straight-edged rupture along their walls and an often planar outline suggest formation by localized pedogenesis along fractures.

The last visible traces of disturbed sediments occur at a depth of 9 m as dikes of angular clasts (mm to cm in scale) of stiff, compressed, black soil (sample C8_9m, Figs. 3 and 7). At a depth of 9 m, a chunk 7 cm in size of rust-colored, pale sediment (sample C8_9m_B) was collected for geochemical analysis. Similar rust-colored chunks were also collected

from a depth of 3 m at crater C9 (sample C9_3m), which at this stage of the machine excavation of C8 had been partly consumed by the excavated pit. The exact original location of the material is not known as it was reworked during the previous excavation by Ormö et al. (2002).

Heated Material and Age Dating

The radiocarbon ages for soil samples are from Ormö et al. (2002) and listed in Table 1. New age data in this study are that of heated clay (TL) and charcoal from C8. In the bowl-shaped section of C8, there was a high content of dispersed fragments of charcoal (sample C8_charcoal_1.8) and small pieces of reddish, heated clay (Figs. 4 and 5). The fragments of heated clay are irregular, lack distinct shapes,

and are full of impurities and vugs. They are of very poor strength and most often occur as grains giving a red stain to the dark soil (Fig. 5a4). The largest and most solid piece was found at a depth of 2.2 m (sample C8_T1_2.2, Fig. 5a1). The ages of the charcoal and heated clay sample C8_T1_2.2 are given in Table 1. The re-firing in connection to the TL analysis of the heated clay sample gave that the material had been heated to a temperature between 900 °C and 1000 °C. No color change was observed at lower re-firing temperatures. The estimated temperature appears high in view of the poor coherence of the heated material. This can be explained by the lack of minerals such as kaolinite and smectite that can enhance the cohesiveness of fired clay materials. An X-ray diffraction analysis showed the dominant clay mineral to be illite.

The residue after the acid treatment of sample Sirente-3 from the rim of the main crater does also contain abundant, reddish-yellowish, mm-size fragments of rust-colored, heated clay material (Fig. 5b), similar to the fragments found in craters C8 (Fig. 5a) and C9, as well as spherical objects referred to as "rusty crusts with rare nickel granules" by Ormö et al. (2002) (Fig. 5c). In addition, the residue contains some organic material, feldspars, pyroxene, and magnetite.

Geochemistry

The results of our measurements are presented in Table 2. The major element contents are typical of clay and/or carbonate-rich (and quartz-poor) materials. The trace element contents show clear evidence of water interaction and precipitation of some sulfide material, as indicated by elevated As and Sb contents. One of the samples (Sirente-3-Residue) has a Ce anomaly, indicating aqueous alteration by weathering. Even though some Cr, Co, and Ni values were higher than others, no obvious or systematic enrichment in siderophile element contents was found in any of the samples.

DISCUSSION

The Search for Traces of Meteoritic Material

Numerical simulations have shown that more than 95% of impact craters of the size of the Sirente main crater are formed by iron meteorites (Bland and Artemieva 2003a, 2006). Most small stony projectiles do not survive the passage through the atmosphere. Often a stony meteorite signature means a chondritic signature, whereas iron meteorites have a much more varied composition (e.g., Buchwald 1975; Mason 1979). Elevated Co or Ni contents do not necessarily correlate with elevated Ir contents in all iron meteorites, even though bulk Ni contents for the various classes range from about 5 to 25 wt% (with an average of about 8 wt%) (Buchwald 1975). Iridium contents of iron meteorites are equally variable, ranging from a few ppb to about 100 ppm. Thus, it is possible to have an iron meteorite that has 10 wt% Ni and 20 ppb Ir,

and another that has 6 wt% Ni and 10 ppm Ir. In such a young and small structure, mechanical breakup (and weathering) of meteorite fragments would dominate. The formation of melt and vapor is not expected due to the small size and low impact velocity (e.g., Collins et al. 2005), although ablated material formed during passage through the atmosphere could be dispersed in the crater-related materials. If the Sirente structure had formed by meteoritic impact, meteoritic contamination of the target sediments would mainly occur in direct contact with the meteoritic fragments and possibly in material affected by fall-out from ablation. The high Cr values in some of our samples cannot be of extraterrestrial origin because of the very low probability of a stony impactor and high associated As, Sb, and V values, which are typical of non-meteoritic sources. Only one sample, Sirente-4, yielded an Ir value barely above the detection limit (about 0.1 ppb); this low value was measurable because the sample was carbonate-rich and had low contents of interfering elements, and was counted for three days in the final counting step. However, this value is at about the detection limit for Ir in this particular sample, and, thus, no analytical significance can be attached to it. Detection limits for Ir in other samples are <0.2 to <1.5 ppb.

Taking an Ni content of 70 ppm and a Co content of 20 ppm (samples C8_TC2 and C9_3m) and subtracting an average indigenous content of about 8 and 6 ppm, respectively, we arrive at 62 and 14 ppm, respectively. For the average iron meteorite Ni and Co contents of 8 and 0.5 wt%, respectively, this would mean a meteoritic component of about 0.1 to 0.3 wt% in samples C8_TC2 and C9_3m. Given a range of possible Ir values of 10 ppb to 100 ppm, for such a meteoritic component we would then expect a range of 0.01 to 100 ppb Ir. The lower range is below the detection limit of the INAA method (~0.1–1 ppb, depending on sample and counting parameters), and would not be characteristic anyway (not high enough above terrestrial background), and the higher values are clearly not present. In our case, we were unable to detect statistically significant Ir contents in any of our samples. This is further amplified by the expectation of weathered meteorite fragments at such a small structure, which should then contain a much higher meteoritic component than 0.3 wt%. We therefore conclude that there is no obvious and unambiguous meteoritic signature in the analyzed samples, but its presence also cannot be categorically excluded.

Subsurface Structure, Heated Material, and Significance of Age Determinations

Here we discuss both the age determinations done in this study and the previous ages presented by Ormö et al. (2002). The only age that can be directly linked to the formation of one of the craters is that from the paleosol ("target surface") on top of which the material of the main crater rim has been deposited (Sample DH2[1.5]). This is independent of

Table 2. Compositions of samples from the Sirente crater field[a].

	C8_TC2	C9_3m	Sirente-3_bulk	Sirente-4	C8_Ref	C8_9m_B	Sirente-3_residue
SiO_2	45.96	48.59	8.67	18.05	5.67	7.41	
TiO_2	1.01	1.00	0.21	0.43	0.15	0.16	
Al_2O_3	21.26	21.95	4.03	8.89	2.54	3.50	
Fe_2O_3	7.98	8.00	1.47	3.04	0.89	0.97	12.54
MnO	0.18	0.14	0.04	0.05	0.03	0.05	
MgO	1.61	1.77	0.75	1.00	0.69	0.65	
CaO	1.59	1.80	46.79	35.09	50.44	48.38	
Na_2O	0.47	0.45	0.07	0.16	0.06	0.22	0.55
K_2O	2.29	2.53	0.28	0.76	0.25	0.46	2.36
P_2O_5	0.67	0.39	0.13	0.28	0.07	0.08	
LOI	16.83	12.74	37.83	32.69	39.03	37.88	
Total	99.85	99.36	100.27	100.44	99.82	99.76	
Sc	18.3	16.5	3.37	7.17	1.99	1.83	18.6
V	188	194	29	54	24	25	n.d.
Cr	127	115	23.5	49.4	14.0	12.2	125
Co	19.8	18.8	4.35	7.95	8.52	2.42	31.1
Ni	68	75	8	6	8	10	62
Cu	48	40	<9	14	<9	<9	n.d.
Zn	169	145	38	243	17	27	107
As	17.1	12.9	3.11	6.35	2.17	3.96	37.8
Se	0.7	0.4	0.2	0.2	0.1	0.1	0.4
Br	6.5	5.5	0.9	0.9	0.4	0.4	1.5
Rb	250	180	38.3	95.9	20.0	31.7	118
Sr	102	123	109	104	117	114	360
Y	48	53	13	21	10	13	n.d.
Zr	282	307	52	112	29	104	310
Nb	35	34	9	15	6	17	n.d.
Sb	0.77	0.89	0.11	0.28	0.10	0.11	0.51
Cs	19.8	19.9	4.06	8.26	2.35	3.21	7.71
Ba	655	542	63	141	47	56	390
La	89.3	96.2	16.7	38.9	11.5	25.1	38.3
Ce	160	160	33.8	65.2	19.5	43.2	121
Nd	70.8	74.4	15.2	31.2	8.78	15.8	41.1
Sm	11.8	12.4	1.95	5.16	1.50	2.27	7.85
Eu	2.57	2.45	0.55	1.09	0.33	0.38	1.75
Gd	11.5	11.6	2.1	4.4	1.3	2.8	6.5
Tb	1.61	1.44	0.27	0.59	0.18	0.36	0.84
Tm	0.78	0.72	0.14	0.32	0.077	0.23	0.41
Yb	4.44	4.66	0.82	2.02	0.62	1.43	2.53
Lu	0.70	0.71	0.12	0.28	0.088	0.22	0.37
Hf	8.26	8.19	1.65	3.33	0.98	2.55	8.21
Ta	1.93	1.71	0.37	0.75	0.21	0.75	1.13
W	10.6	8.7	1.3	4.1	0.9	2.8	7.9
Ir (ppb)	<1.6	<0.4	<0.4	0.1	<0.3	<0.2	<0.6
Au (ppb)	<0.9	<1	0.4	0.7	0.5	0.7	0.7
Th	34.9	36.3	7.40	14.9	4.35	12.4	17.4
U	3.31	3.35	0.67	1.05	0.51	0.42	1.36
K/U	6918	7552	4179	7238	4902	10,952	17,353
Zr/Hf	34.1	37.5	31.5	33.6	29.6	40.8	37.8
La/Th	2.56	2.65	2.26	2.61	2.64	2.02	2.20
Th/U	10.5	10.8	11.0	14.2	8.5	29.5	12.8
LaN/YbN	13.6	14.0	13.8	13.0	12.5	11.9	10.2
Eu/Eu*	0.67	0.62	0.83	0.70	0.72	0.46	0.75

[a]Major element data in wt%. Trace elements in ppm except as noted.

whatever process, human or natural, that caused the displacement of the material. Sample DH2(1.5) is constrained by the ages of samples DH2(0.9) and DH2(2.0) occurring immediately above and below (see Fig. 7 in Ormö et al. 2002). Stoppa (2006) argue that the discovery of a 1st century A.D. Roman coin at the surface of the main crater rim puts the formation further back in time. However, the coin would only be of significance if it had been found below the material of the elevated rim. In that case it would give a maximum age of formation, nevertheless still not excluding the age suggested by Ormö et al. (2002) (Table 1). Furthermore, Stoppa (2006) clearly states that the rim itself does not contain artifacts. Speranza et al. (2004) argue that the relatively high age for sample C9(3.5)org in crater C9 would exclude a contemporaneous formation of the crater field and, thus, the impact hypothesis. However, sample C9(3.5)org does not give the absolute age of formation of crater C9, only its maximum age. The sample is a fragment of organic soil formed by the disruption of a soil horizon predating the formation of the crater, whatever the cause of formation (see Fig. 4 in Ormö et al. 2002). The age of C9(3.5)org together with the age of sample DH2(1.5) were used by Ormö et al. (2002) to exclude some alternative causes of formation that required a very high age (e.g., periglacial structure).

The TL and radiocarbon ages listed in Table 1 are the best possible ages obtainable with current samples and methods for constraining the age of the crater field, whatever the cause of its formation. In addition to the errors related to the measurements themselves, there is a natural error as well: the radiocarbon dating gives the age when an organic object died (stopped incorporating the ^{14}C isotope). Hence, in the case of the charcoal sample, it does not necessarily date the time the object was heated, which would be of interest for an exact dating of the putative impact event. The TL gives the age when the clay was heated, but with wide error margins. Thus, so far, only for the main crater it can be said that the formation has been dated. The apparent close proximity of the ages of C8 and the main crater suggests a simultaneous formation, but it is not proven. Nevertheless, none of the ages excludes a simultaneous formation of the craters.

Impact velocities for funnel craters have been estimated to be fairly high: 3.7 km/s for the Campo del Cielo (Cassidy and Renard 1996), 2–4 km/s for Sterlitamak (Ivanov and Petaev 1992), and 1–3 km/s for the funnel-shaped craters at Sikhote Alin (Svettsov 1998). However, recent numerical simulations indicate that the most common velocity is about 1 km/s (Bland and Artemieva 2006). Experiments to create craters several meters wide from missile impacts have shown partial fusion of the missiles at impact velocities of 3.9 km/s (Moore 1976). It should thus be possible to achieve the temperatures needed to generate heated clay and charcoal at C8, at least for a small amount of the target. A porous target adds to the transfer of kinetic energy to heat (Melosh 1989; Wünnemann and Collins 2006). Recent
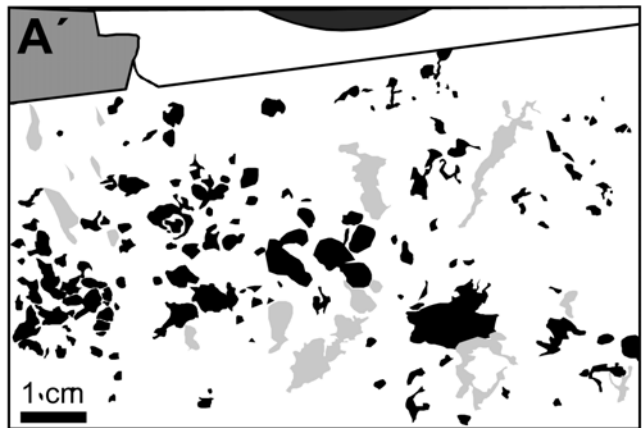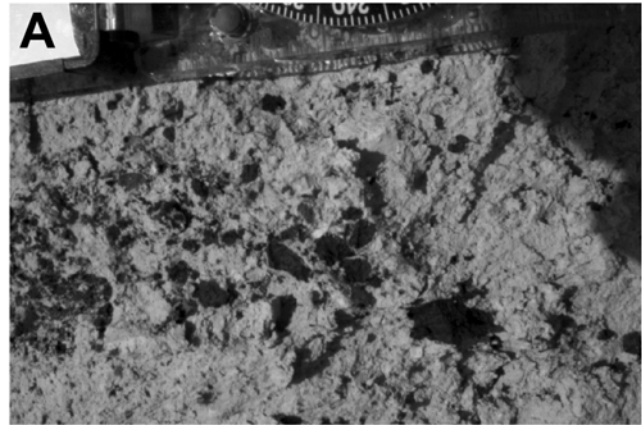

Fig. 7. Dike of injected fragments of angular, hard, compressed dark soil at 9 m depth below crater C8. It represents the deepest encountered trace of the apparent "tunnel" (see Fig. 3). Irregular pale-grey areas in line drawing (A') indicate shadows in the photo in (A). Black areas indicate soil fragments.

studies of Campo del Cielo show occurrences of reddish clay within the crater structures in close association with the meteorites. The red material is interpreted to be a result of baked earth and subsequent weathering products of the iron and silicate inclusions (Wright et al. 2006). The occurrence of reddish, baked earth is shared with many more small impact craters around the world (see list below). Thus, it is possible that the heated clay and charcoal at C8 formed by impact heating.

The absence of heated clay and "rusty crusts" in reference samples of similar composition from the plain indicates that the fragments found in the main crater rim may be linked to its formation. When clay is heated to a temperature of >600 °C, it loses its chemically bonded water and can no longer be broken down by water. The heated clay and rusty crusts are the only equivalents to fused material found so far. Heating of the carbonate mud may not form spherules such as in more silica-rich targets. When heated, the mud turns into CO_2 and CaO. If exposed to water (e.g., rainfall), the CaO will react and form $Ca(OH)_2$. This will

again react with CO_2 and quickly change back into the same calcium carbonate as before the heating. Hence, the chances of finding fused material with a meteoritic component at Sirente are small.

Plausible non-impact formation of the heated material would be brushfires or camp fires. Studies of soil temperature at brushfires have shown that temperatures above 600 °C are sustained for several hours in the uppermost centimeter of the ground (Odion and Davis 2000). Below a depth of 2 cm, the temperatures never reach above 150 °C. The heated clay and charcoal in C8 could, if formed by brushfires, have constituted a layer that either existed before the formation of C8 and got relocated (e.g., by karstic collapse), or that formed after the C8 and accumulated in an already existing depression. What argues against such a scenario is that the heated material has only been observed (and is quite apparent) in the main crater rim and within the infill of C8 and C9, but not during careful examination of the soil profiles displayed during the 600 m^2 wide machine excavation and in Pit 1. The dispersed distribution of the heated material in most of the infill of C8 also indicates a generation of the heated material either before or during the formation of C8, rather than the single layer expected if accumulated within an existing depression. The well-dispersed, mm-size fragments of heated clay at all sample locations in the main crater rim argues for a syn- or post-heating physical process capable of dispersing fine-grained heated material into the bulk of the rim material. This widespread appearance of the heated material would not be expected if caused by localized campfires.

The apparent very steep dip of C8's tunnel is inconsistent with the most common angle of trajectory in hypervelocity impacts (45°) (Melosh 1989). However, steep angles (<10° from the vertical) were observed at several funnel craters at Sikhote Alin (Svettsov 1998). The layer of soil breccia outside crater C8 has not been detected elsewhere in sections through the upper sediments of the plain during the machine excavation, which was 3 m deep and 600 m^2 wide (first platform), as would be expected if caused by agricultural plowing. Hence, the sheared breccia layer may represent traces of a downrange ejecta layer. Stoppa (2006) used aerial photos to recognize extensive lobate deposits extruding from the main crater. Their distribution, mainly to the southeast, coincides with the distribution of the soil breccia on the southeastern side of C8. This, combined with the elongation and saddle-shaped rim of the main crater and the outline of the crater field (cf. Ormö et al. 2002; this study), would suggest them to be downrange ejecta deposits from an impact from the northwest. With respect to the target being a wet mud and not solid rock, and the expected low impact velocity resulting in an excavation flow driven rather by a mechanical push than acceleration by shock, it is possible that the ejecta could at least partly be emplaced as fluidized ejecta (cf. Carr et al. 1977; Barlow

2005) rather than ballistic ejecta. However, Stoppa (2006) excludes the deposits to be of impact origin and instead favors a formation by gravity-driven flows from a mud volcano. He does, however, notice a problem in why the flows have flowed toward the higher ground southeast of the crater and not toward the lower ground in the northwest.

Outline of the Proposed Crater Field Compared to Confirmed Crater Fields

The lack of unequivocal evidence for a meteoritic impact notwithstanding, a comparison between the possible crater field of Sirente and known impact crater fields is important when analyzing the significance of the geological observations. We here list known impact sites with craters similar to the size of the Sirente main crater, based on the review by Hodge (1994) and additional references. Notable is that several have yielded very little meteoritic material, especially those located in areas with long history of iron working (cf. the Americas and Australasia where iron working was introduced by European colonists in recent historic time). Human overprint on meteorite craters is expected, as illustrated by extensive constructions at and within the Kaali main crater (Veski et al. 2001). The Sirente plain is characterized by a humid climate and sediment deposition rather than erosion; thus any remaining fragments, as well as an ablation fallout layer with geochemical traces of the impactor, would be buried under 0.5–1 m of younger sediments. For comparison with the Sirente structure, we have illustrated three crater fields with a similar outline in Fig. 1.

Craters with No Documented Satellite Craters
- Boxhole (Australia), 185 m in diameter, common iron meteorites in the surroundings, but very rare melt spherules in soil. Age: ~5 kyr (Hodge 1994), ~30 kyr (Shoemaker et al. 1990).
- Veevers (Australia), 80 m in diameter. Iron meteorite fragments occur off the northeast rim. Age: <1 Myr.
- Sterlitamak (Russia). A funnel-shaped crater 10 m wide, formed by an iron meteorite fall in 1990 (Petaev 1992). Only 20% of the calculated weight of the impactor was retrieved, mostly from the end of the "funnel" at a depth of 12 m. Large high-density lumps of reddish loams occur within the tube-shaped bottom of the funnel.
- Haviland (Kansas, USA). Originally elliptical crater (17 × 10.7 m), but now destroyed by cultivation. Long used as cattle pond because it, in analogy with Sirente, holds water in an otherwise permeable sediment. Common iron meteorite fragments in cone-shaped layer along the true crater floor. The deepest fragment discovered during excavation was at 2.9 m depth. All fragments were surrounded by rust-colored soil. Age: <1 kyr.

- Dalgaranga (Australia). A crater 20 m wide with common meteoritic (mesosiderite) fragments, mainly to the southwest of the crater. Age: ~25 kyr (Hodge 1994), ~0.27 Myr (Shoemaker et al. 1990).
- Sobolev (Russia). A 50 m crater. No reported meteorite fragments, but nickel-rich spherules have been recovered. Age: ~0.2 kyr.

Craters with a Bimodal Size Distribution (Distinct Main Crater with Much Smaller Satellite Craters)
- Odessa (Texas, USA). Main crater 170 m in diameter, and 3–4 smaller craters, the largest with a diameter of 25 m (Fig. 1). Iron meteorites are common below the crater infill, at the rim, and in the surroundings. Spherules in soil samples. Previous age of <50 kyr has been revised to 63.5 ± 4.5 kyr (Holliday et al. 2005).
- Kaali (Estonia). One main crater (110 m) and eight smaller craters located to the south of the main crater (39 m, 36 m, 33 m, 26 m, 25 m, 20 m, 13 m, and one small indistinct) (Fig. 1). Iron meteorite. Only a total of 2.5 kg meteoritic fragments have been collected, the largest the size of a fingertip and only weighing about 30 g (Veski et al. 2001). Microscopic meteorite material and glassy spherules occur in sediments at the field (Koval 1980; Smith and Hodge 1993) and iridium anomalies have been reported from nearby swamps and have been used in an attempt to date the event (800–400 B.C.) (Veski et al. 2001), although other ages have been suggested as well (Raukas 2000).
- Morasko (Poland). A main crater 100 m wide surrounded on all sides by smaller craters (63 m, 50 m, 35 m, 35 m, 25 m, 24 m, and 15 m). Iron meteorites have been found during trenching. Microscopic meteorite particles found mainly near the main crater. Age: ~10 kyr.
- Wabar (Saudi Arabia). Shoemaker and Wynn (1997) describe three craters, 100, 64, and 11 m in width. Silica-rich target (desert sands). Iron meteorite fragments and impact glass with meteoritic component occur at the site (Prescott et al. 2004). Age: 6 kyr (Hodge 1994), ~0.3 kyr (Prescott et al. 2004).
- Macha (Russia). A doublet structure consisting of a 300 m-wide crater intersected by a crater 180 m wide (Gurov and Gurova 1998). Three craters 60–90 m wide are located on one side of the doublet. Planar fractures in quartz and microscopic metallic particles that are high in iron and iridium, but low in nickel and cobalt confirm the impact origin. No macroscopic meteorites have yet been reported. Chunks of red burnt clay occur within the craters. Age: ~7 kyr.

Crater Fields with a Wider Distribution of Crater Sizes
- Henbury (Australia). The mean diameters (elliptical) of the mapped craters are (Milton 1968): 180 × 140 m (the "main crater" comprises two smaller craters, 160 m and 130 m respectively), plus at least a dozen smaller structures with diameters from 7 to 100 m (Fig. 1). Iron meteorite fragments and impact glass occur in the area. Age: <5 kyr.
- Campo del Cielo (Argentina). Field of craters from extremely oblique impact (9°) (Cassidy and Renard 1996). Nine craters (mostly elliptic) with diameters from 115 to 20 m were found. Large pieces (tons) of iron meteorites found mainly within the boundaries of the craters, often at the end of many meters long, sometimes curved, penetration shafts (highly oblique funnel shapes). Reddish baked earth occurs within the craters in close proximity with the meteorites (Wright et al. 2006). Age: <4 kyr.
- Ilumetsa (Estonia). The diameters of the mapped craters are 80, 50, and 24 m. No reported meteorite fragments. A layer of possible impact spherules in a nearby bog has been used as a proof of the impact origin and in an attempt to date the event (~6 kyr) (Raukas et al. 2001).
- Sikhote Alin (Russia). Formed by iron meteorite fall in 1947 and has 122 craters larger than 0.5 m, the largest being 27 m in diameter. The meteorites forming the largest craters suffered explosive disruption at impact and are left as fragments in the crater infill. The smaller craters often have a funnel shape with intact projectiles at the end of the funnel (up to 8 m in length).

The main crater often occurs at the end of the field due to aerodynamic size sorting (see Melosh 1989 and references therein) and is most often formed by a cluster of projectiles (Bland and Artemieva 2003a, 2006). Numerical simulations of crater fields (Bland and Artemieva 2003a, 2003b, 2006) show a complete spectrum of fragment sizes that increase gradually towards the main crater(s), however, with clusters forming individual larger craters explaining the nonlinear size distribution in some crater fields. The distribution of the craters at crater fields such as Henbury, Kaali, and Odessa, with some distance between the main crater and the satellite craters (Fig. 1), is of more interest in the comparisons with the Sirente crater field. Maybe it is a consequence of strength variations in the meteoroid affecting the atmospheric breakup. The outline of the Sirente crater field is thus more similar to some crater fields with a large single crater surrounded by much smaller satellite craters (Fig. 1) than crater fields with large number of small craters (e.g., Sikhote Alin).

CONCLUSIONS

Detailed mapping shows a field of craters with dimensions and outline consistent with known crater fields with a large main crater. No unambiguous evidence of the presence of meteoritic material was found, either macroscopically or in the form of geochemical anomalies in the analyzed samples. Machine excavation of one of the putative satellite craters (C8) shows a funnel-shaped structure approximately 8 m wide, narrowing strongly and apparently disappearing downward, and with indications for surface soil

injection to a depth of at least 9 m. Outside the apparent rim of C8 there are evidence of possible ejecta. Charcoal and small, irregular fragments of heated clay from the crater infill have calibrated ages of B.P. 1712 (^{13}C-corrected radiocarbon age: B.P. 1800 ± 100) for the charcoal, and B.P. 1825 (calculated error ± 274) for the clay. The new ages and the previously published age of the main crater (B.P. 1538) indicate a formation of the crater field at the beginning of the first millennium A.D. Small fragments of heated clay are also common in the rim material of the main crater, but have not been found elsewhere in the sediments of the plain. The age correlations, morphology of the main crater, structure of C8 and C9, heated material, and outline of the crater field are consistent with, but do not unambiguously confirm, the impact hypothesis. Regardless of the ultimate outcome of the discussion, the Sirente crater field is an important point of reference in comparison with small, meteorite-generated crater fields on Earth.

REFERENCES

Aitken M. J. 1976. Thermoluminescent age evaluation and assessment of error limits: Revised system. *Archaeometry* 18: 233–238.

Aitken M. J. 1985. *Thermoluminescence dating.* London: Academic Press. 359 p.

Barlow N. G. 2005. A review of Martian impact crater ejecta structures and their implications for target properties. In *Large meteorite impacts III,* edited by Kenkmann T., Hörz F., and Deutsch A. Boulder, Colorado: Geological Society of America. pp. 433–442.

Bland P. A. and Artemieva N. A. 2003a. Efficient disruption of small asteroids by Earth's atmosphere. *Nature* 424:288–291.

Bland P. A. and Artemieva N. A. 2003b. The impact rate of small asteroids at the Earth's surface (abstract #4047). 3rd International Conference on Large Meteorite Impacts. CD-ROM.

Bland P. A. and Artemieva N. A. 2006. The rate of small impacts on Earth. *Meteoritics & Planetary Science* 41:607–631.

Buchwald V. F. 1975. *Handbook of iron meteorites: History, distribution, composition and structure.* Berkeley: University of California Press. 1418 p.

Carr M. H., Crumpler L. S., Cutts J. A., Greeley R., Guest J. E., and Masursky H. 1977. Martian impact craters and the emplacement of ejecta by surface flow. *Journal of Geophysical Research* 82: 4055–4065.

Cassidy W. A. and Renard M. L. 1996. Discovering research value in the Campo del Cielo, Argentina, meteorite craters. *Meteoritics & Planetary Science* 31:433–448.

Collins G. S., Melosh H. J., and Marcus R. A. 2005. Earth impact effects program: A web-based computer program for calculating the regional environmental consequences of a meteoroid impact on Earth. *Meteoritics & Planetary Science* 40:817–840.

Commissariato per la reintegra dei tratturi di Foggia. 1959. Carta dei Tratturi, Tratturelli, Bracci e Riposi, updated in 1959, based on 1911 version of the map. Litografia Artistica Cartografica, Firenze, Italy. Scale 1:500,000.

Daszkiewicz M. and Schneider G. 2001. Klassifizierung von Keramik durch Nachbrennen von Scherben. *Zeitschrift für Schweizerische Archäologie und Kunstgeschichte* 58:25–32.

Evans G. L. 1961. Investigations at the Odessa meteor craters. Lawrence Radiation Laboratory Report UCRL-6438, pt. 1, Paper D. Livermore: University of California. 11 p.

French B. M. 1998. *Traces of catastrophe: A handbook of shock-metamorphic effects in terrestrial meteorite impact structures.* Houston, Texas: Lunar and Planetary Institute. 120 p.

Giraudi C. 1997. Late Pleistocene and Holocene level fluctuations of the ephemeral lake of the Pezza Plain (Abruzzo, Central Italy) (with abstract in English). *Il Quaternario, Italian Journal of Quaternary Science* 10:191–200.

Gurov E. P. and Gurova E. P. 1998. The group of Macha craters in western Yakutia. *Planetary and Space Science* 46:323–328.

Hodge P. 1994. *Meteorite craters and impact structures of the Earth.* Cambridge: Cambridge University Press. 124 p.

Holliday V. T., Kring D. A., Mayer J. H., and Goble R. J. 2005. Age and effects of the Odessa meteorite impact, western Texas, USA. *Geology* 33:945–948.

Ivanov B. A. and Petaev M. I. 1992. Mass and impact velocity of the meteorite formed the Sterlitamak crater in 1990 (abstract). 22nd Lunar and Planetary Science Conference. pp. 573–574.

Kenkmann T. and Dresen G. 1998. Stress gradients around porphyroclasts: Palaeopiezometric estimates and numerical modelling. *Journal of Structural Geology* 20:163–173.

Koeberl C. 1993. Instrumental neutron activation analysis of geochemical and cosmochemical samples: A fast and reliable method for small sample analysis. *Journal of Radioanalytical and Nuclear Chemistry* 168:47–60.

Koeberl C., Reimold W. U., and Shirey S. B. 1998. The Aouelloul crater, Mauritania: On the problem of confirming the impact origin of a small crater. *Meteoritics & Planetary Science* 33: 513–517.

Koval V. I. 1980. Finely dispersed material from the Kaali meteorite crater field. *Solar System Research (Astronomicheskii Vestnik)* 14:80–87.

Mason B. 1979. Meteorites. In *Data of geochemistry, Chapter B– Cosmochemistry.* U.S. Geological Survey Professional Paper #440-B-1. Reston, Virginia: United States Government Printing Office. pp. 117–120.

Melosh H. J. 1989. *Impact cratering: A geologic process.* New York: Oxford University Press. 245 p.

Milton D. J. 1968. Structural geology of the Henbury meteorite craters, Northern Territory, Australia. U.S. Geological Survey Professional Paper #599-C. Washington, D.C.: United States Government Printing Office. 17 p.

Montanari A. and Koeberl C. 2000. *Impact stratigraphy: The Italian record.* Heidelberg: Springer-Verlag. 364 p.

Moore H. J. 1976. Missile impact craters (White Sands Missile Range, New Mexico) and applications to lunar research.

Contributions to Astrogeology. U.S. Geological Survey Professional Paper #812-B. Washington, D.C.: United States Government Printing Office. 47 p.

Nambi K. V. S. and Aitken M. J. 1986. Annual dose conversion factors for TL and ESR dating. *Archaeometry* 28:202–205.

Odion D. C. and Davis F. W. 2000. Fire, soil heating, and the formation of vegetation patterns in chaparral. *Ecological Monographs* 70:149–169.

Ormö J., Rossi A. P., and Komatsu G. 2002. The Sirente crater field, Italy. *Meteoritics & Planetary Science* 37:1507–1521.

Petaev M. I. 1992. The Sterlitamak meteorite: A new crater-forming fall. *Solar System Research (Astronomicheskii Vestnik)* 26:82–99.

Prescott J. R., Robertson G. B., Shoemaker C., Shoemaker E. M., and Wynn J. 2004. Luminescence dating of the Wabar meteorite craters, Saudi Arabia. *Journal of Geophysical Research* doi: 10.1029/2003JE002136. 8 p.

Raukas A. 2000. Investigation of impact spherules—A new promising method for the correlation of Quaternary deposits. *Quaternary International* 68–71:241–252.

Raukas A., Tiirmaa R., Kaup E., and Kimmel K. 2001. The age of the Ilumetsa meteorite craters in southeast Estonia. *Meteoritics & Planetary Science* 36:1507–1514.

Reimold W. U., Koeberl C., and Bishop J. 1994. Roter Kamm impact crater, Namibia: Geochemistry of basement rocks and breccias. *Geochimica et Cosmochimica Acta* 58:2689–2710.

Santilli R., Ormö J., Rossi A. P., and Komatsu G. 2003. A catastrophe remembered: A meteorite impact of the 5th century A.D. in the Abruzzo, central Italy. *Antiquity* 77:313–320.

Servizio Geologico d'Italia-APAT 2004. Forthcoming. Foglio N. 368 "Avezzano" della Carta Geologica d'Italia a scala 1:50.000 e note illustrative (Geological map of Italy, sheet no. 368). Servizio Geologico d'Italia—Istituto Poligrafico e Zecca dello Stato (Italian Geological Survey), Roma.

Shoemaker E. M., and Wynn J. C. 1997. Geology of the Wabar meteorite craters, Saudi Arabia (abstract #1075). 28th Lunar and Planetary Science Conference. CD-ROM.

Shoemaker E. M., Shoemaker C. S., Nishiizumi K., Kohl C. P., Arnold J. R., Klein J., Fink D., Middleton R., Kubik P. W., and Sharma P. 1990. Ages of Australian meteorite craters—A preliminary report (abstract). *Meteoritics* 25:409.

Smith T. R. and Hodge P. W. 1993. Microscopic meteorite material surrounding meteorite craters (abstract). *Meteoritics* 28:439.

Soprintendenza per i Beni Archeologici per L'Abruzzo. 2004. Cartographic database based on 1:25,000 maps (Istituto Geografico Militare) of archeological sites, archeological areas, tratturi, tratturelli, bracci, and riposi, and on 1:2000 maps (Catasto—Land Register Maps), Soprintendenza per i Beni Archeologici per l'Abruzzo, Chieti (Italy).

Speranza F., Sagnotti L., and Rochette P. 2004. An anthropogenic origin of the "Sirente crater," Abruzzi, Italy. *Meteoritics & Planetary Science* 39:635–649.

Stoppa F. 2006. The Sirente crater, Italy: Impact versus mud volcano origins. *Meteoritics & Planetary Science* 41:467–477.

Stuiver M. and Reimer P. J. 1993. Extended ^{14}C database and revised CALIB 3.0 ^{14}C age calibration program. *Radiocarbon* 35:215–230.

Stuiver M., Reimer P. J., Bard E., Beck J. W., Burr G. S., Hughen K. A., Kromer B., McCormac G., van der Plicht J., and Spurk M. 1998. INTCAL98 radiocarbon age calibration, 24000-0 cal BP. *Radiocarbon* 40:1041–1083.

Svettsov V. V. 1998. Enigmas of the Sikhote Alin crater field. *Solar System Research* 32:67–78.

Veski S., Heinsalu A., Kirsimäe K., Poska A., and Saarse L. 2001. Ecological catastrophe in connection with the impact of the Kaali meteorite about 800–400 B.C. on the island of Saaremaa, Estonia. *Meteoritics & Planetary Science* 36:1367–1375.

Wright S. P., Vesconi M. A., Gustin A., Williams K. K., Ocampo A. C., and Cassidy W. A. 2006. Revisiting the Campo del Cielo, Argentina crater field: A new data point from a natural laboratory of multiple low velocity, oblique impacts (abstract #1102). 37th Lunar and Planetary Science Conference. CD-ROM.

Wünnemann K. and Collins G. S. 2006. The effect of porosity on meteorite impact processes (abstract #03991). Geophysical Research Abstracts 8. CD-ROM.